Construction and Building Materials 306 (2021) 124831

Contents lists available at ScienceDirect

Construction and Building Materials

journal homepage: www.elsevier.com/locate/conbuildmat

Investigating the cracking of plastered stone masonry walls under shear–compression loading

Amir Rezaie [a], Michele Godio [b], Katrin Beyer [a,*]

[a] Laboratory of Earthquake Engineering and Structural Dynamics (EESD), School of Architecture, Civil and Environmental Engineering (ENAC), École Polytechnique Fédérale de Lausanne (EPFL), 1015 Lausanne, Switzerland

[b] RISE Research Institutes of Sweden, Brinellgatan 4, 504 62 Borås, Sweden

ARTICLE INFO

Keywords:
Masonry
Crack width
Digital image correlation
Deep learning
Post-earthquake assessment

ABSTRACT

Cracks are the most important source of information about the damage that occurs to unreinforced masonry piers under seismic actions. To predict the structural state of unreinforced masonry piers after an earthquake, research models have been developed to quantify important features of crack patterns. One of the most used crack features is the width, but this can be influenced by several parameters such as the axial load ratio, the shear span ratio, and the loading protocol, which have not been fully studied in previous research studies.

In this study, we use experimental data to investigate the evolution of cracking in stone masonry piers during the application of cyclic shear–compression loading. The data consists of gray-scale images taken during quasi-static shear–compression tests performed on six plastered rubble-stone masonry walls subjected to constant axial force and cycles of increasing drift demand. Through the combined use of digital image correlation and a pre-trained deep learning model, crack pixels are identified, post-processed, and quantified based on their width. The dependency of the crack width on the axial load ratio, the shear span ratio, and the loading protocol at the peak force and ultimate drift limit states of the piers is clarified by a displacement vector field analysis, histogram of the crack width, and the concentration of deformation in the cracks.

We show that, as opposed to flexural cracks, diagonal shear cracks do not fully close when moving from the applied drift demand to the residual drift measured upon removal of the lateral load. Furthermore, we provide the maximum residual crack width at peak force and ultimate drift limit states. This study will improve the decision making abilities of future models used to quantify earthquake-induced damage to stone masonry buildings.

1. Introduction

Stone masonry buildings have shown poor performance in previous earthquakes [1]. According to FEMA 306 [2], usability and serviceability of a damaged building can be assessed based on the severity and type of damage. In brittle construction materials, like masonry and concrete, cracks are the primary source of information on the damage severity. They are used to build empirical and physics-based models to classify the failure mode and estimate their residual capacity [3–8]. Below we summarize the studies that used crack pattern features within the scope of damage assessment of brittle structural elements.

Several studies link a qualitative description of the crack pattern and maximum crack width to the maximum displacement ductility that the structural system has attained [9–12]. For assessing the severity of cracking in a structural member, the prime criteria are the crack orientation and maximum crack width [2]. In addition, the following other criteria have been used in the literature to quantify the extent of cracking in a structural member: crack length [8,13,14], crack density [14,15], a dimensionless quantity combining the number of cracks and their width and length [16,17], fractal and multifractal characteristics of crack patterns [6,7,18–23], and crack size [5]. FEMA 306 [2] recommends classifying the damage level using the crack width, the extent of the cracked area, and the type of crack (oriented diagonally or horizontally, stair-stepped, X-shape). In FEMA 306 [2], damage severity in a structural component is classified as insignificant, slight, moderate, heavy, or extreme. Based on these damage grades, modification factors for stiffness, strength, and deformation capacity have been proposed [2]. Similarly, AeDES [24] determines the damage severity (slight, medium–severe, and very heavy) based on the type of crack, the surface crack position, and the crack width. Here, slight

* Corresponding author.
E-mail address: katrin.beyer@epfl.ch (K. Beyer).

https://doi.org/10.1016/j.conbuildmat.2021.124831
Received 2 July 2021; Received in revised form 3 September 2021; Accepted 3 September 2021
Available online 15 September 2021

damage is characterized by flexural or diagonal shear cracks of less than 1 mm in width, and medium–severe damage is characterized by flexural cracks of 10–15 mm or diagonal shear cracks of 2–10 mm in width. Additionally, Novelli and D'Ayala [25] used crack pattern and damage severity to develop a knowledge-based system for the post-earthquake assessment of masonry buildings that would output the failure mode type and its level. Tomaževič [9] proposed a correlation between EMS-98 damage grades [26], limit states, and the crack width information recorded during cyclic shear–compression tests on masonry walls with clay units. Korswagen et al. [16] proposed a dimensionless quantity called damage level parameter (Ψ) that depends on the number of cracks and their length and width. It is empirically defined as:

$$\Psi = 2n_c^{0.15}\hat{c}_w^{0.3}, \tag{1}$$

where n_c is the number of cracks in the specimen, and $\hat{c}_w$ is formulated as:

$$\hat{c}_w = \frac{\sum_{i-1}^{n_c} c_{w,i}^2 c_{L,i}}{\sum_{i-1}^{n_c} c_{w,i} c_{L,i}}. \tag{2}$$

Here, $c_{w,i}$ and $c_{L,i}$ are the maximum width and the length of crack branch i [16]. This quantity was used to track the intensity of damage, independent of specimen size, during in-plane cyclic tests on solid clay-brick specimens [16].

Dolatshahi and Beyer [6] used the notion of fractal dimension to correlate stiffness and strength reduction with the crack patterns observed in shear–compression tests on brick masonry walls conducted by Petry and Beyer [27]. Rezaie et al. [18] showed that the fractal dimension of crack patterns is very sensitive to the settings of the box-counting method used to determine it. The authors proposed a set of recommendations to select the correct set of parameters for computing the fractal dimension of crack patterns on masonry walls.

Most unreinforced masonry buildings have walls covered with layers of plaster, which are sometimes considered as artistic assets. To understand how the damage in plaster is related to the structural damage, a number of studies can be found in the literature. Calderini et al. [28] considered two groups of damage states referencing the structural and non-structural (plaster/artistic asset) components. They found a linear trend between the crack width and the drift of the panel at peak force by analyzing the results of two experimental campaigns on stone masonry panels, namely Genoa's panels and Ljubljana's walls. They found that Genoa's panels never reached the A4 damage limit state (plaster collapse), and, in most of the walls in Ljubljana, the drift at A2 damage state (first visible structural crack on the plaster) was considerably lower than the drift at the FC damage limit state (first structural crack). On average, the ratio of drift at first visible structural crack on the plaster to the drift at first structural crack (on masonry) was around 0.67—a ratio smaller than 1.0 indicates that the structural damage level to the masonry will be overestimated by only considering cracking of plaster. This observation is lower than the values reported by Godio et al. [29] for cyclic tests performed on stone masonry walls that were plastered on one side while left bare on the other. Values between 0.60 and 1.17 were observed in that case (average value of 0.91) and a value of 1 was obtained for most of the walls [29]. A possible reason for this large range of values is that both campaigns visually detected cracks on the unplastered side of the wall, and visual inspection is always prone to error. Furthermore, the properties of the plaster and the characteristics of the bond between the plaster and masonry can have an influence on the drift at plaster cracking. As another alternative, Didier et al. [30] defined two quantities, namely the normalized crack area (NCA) and normalized crack length (NCL) defined in Eqs. (3) and (4), respectively, to quantify the accumulation of damage to plastered clay brick walls tested under cyclic shear–compression loading. In their testing campaign, they used a two-dimensional digital image correlation (DIC) method to obtain the in-plane deformation of specimens. The two quantities are defined as follows:

$$\begin{aligned}\text{NCA} &= \frac{\text{damaged area of the plaster}}{\text{total area of the plaster}} \\ &= \frac{\text{number of white pixels on cumulative von Mises strain map}}{\text{total number of pixels on cumulative von Mises strain map}}.\end{aligned} \tag{3}$$

$$\text{NCL} = \frac{\text{sum of length of all cracks}}{\text{length of wall diagonal}} = \frac{\text{sum of crack perimeters}/2}{\text{length of wall diagonal}}. \tag{4}$$

They obtained the damaged region by setting a threshold on the von Misses strain map to produce a binary image where white pixels represent damage (crack in their study) [30]. They found that the normalized crack area is a better damage descriptor, as it more reliably represents the actual damage than the normalized crack length. Using the normalized cumulative cracked area as a damage measure, Abbiati et al. [31] obtained a probabilistic fatigue model to predict plaster cracking. These studies seem to indicate that plaster cracks almost at the same drift as the masonry.

Xie et al. [32] reviewed existing methods for damage states of infill masonry walls and categorized them into three distinct classes based on: phenomena, force–displacement skeleton curves, and maximum crack width. They tested nine full-scale plastered masonry infilled reinforced concrete frame specimens under cyclic shear–compression loading and obtained the fragility functions with the mentioned methods. They made two important conclusions: (1) defining damage states based on the maximum crack width yielded the least dispersion in the determination of fragility functions; (2) applying plaster did not have a statistically significant effect on the obtained fragility functions. In other words, the maximum crack width observed on both sides of the specimens was almost equal.

From the perspective of repairability of cracks, it is also desirable to use the crack width as a damage variable to define damage limit states. In modern masonry, for cracks with a width of less than 10 mm, Eurocode 8-Part 3 [33] recommends sealing them with mortar or injecting them with cement grout, depending on the thickness of the masonry walls, while epoxy grouting can be used for fine cracks. Otherwise, if the crack width is greater than 10 mm, the damaged area should be reconstructed [33]. It should be pointed out that for historical masonry with lime-based mortar, epoxy grouting is not advised. Vintzileou et al. [34] analyzed the evolution of cracking of brick masonry walls by relating the crack width to the drift demand observed on the walls tested by Petry and Beyer [27,35]. They concluded that the damage is easily repairable up to the point of reaching the force capacity of the wall due to limited crack width [34]. However, when the ultimate drift capacity (20% drop in force) is reached, it is advised to call this near collapse state (from Eurocode 8 - Part 3 [33]) and consider the damage as not easily repairable [34]. This is partly due to the disintegration of masonry, for example, due to X-shaped cracks, and partly to the increase of crack width (up to 9 mm) [34].

Throughout the presented literature, the crack width is mainly selected as the signature for describing a crack network. However, several questions related to the cracking of stone masonry walls under shear–compression loading are still not fully addressed: What is the influence of the loading protocol on the crack width distribution? What is the relationship between the maximum crack width at the maximum drift demand and the residual drift? What is the influence of the shear span and the axial load ratio on the maximum crack width of damaged stone masonry walls? Answering these questions is important and useful from a variety of perspectives: (a) understanding the impact of the above-mentioned parameters on maximum crack width can aid in revising future post-earthquake damage assessment recommendations to include those factors; (b) the relationships between crack width at maximum drift demand and residual crack width can be used to validate numerical models that capture cracking, such as, among others, those

(a) (b)

Fig. 1. (a) Constructed rubble stone masonry walls; (b) application of plaster layers.

developed by Zhang and Beyer [36], Zhang et al. [37], Saloustros et al. [38,39,40]; (c) within the scope of a rapid post-earthquake assessment of damaged masonry buildings using artificial intelligence and image data, the prior incorporation of experimentally verified knowledge can improve predictive models.

In this study, we addressed these topics using the experimental data obtained during quasi-static cyclic shear–compression loading on six large-scale rubble stone masonry walls [41]. We detected and quantified cracks based on images taken systematically from the plastered side of the walls during the loading sequence and processed using DIC. Crack pixels were detected using a deep learning model previously proposed by the authors [42]. The cracks were then skeletonized and cleaned. Finally, the crack width was automatically computed from the DIC outputs for all cracks using an in-house-developed Python script. We used this developed crack detection and quantification pipeline to investigate the above-mentioned questions in greater depth.

The paper is structured as follows: Section 2 explains the experimental data. Section 3 elaborates the steps required to detect, skeletonize, and clean crack networks, and quantify the crack width. Section 4 discusses the previously mentioned questions, and Section 5 summarizes the main findings of this study.

2. Description of experimental tests on stone masonry walls

2.1. Specimens and test program

A conventional experimental test to determine the cyclic performance of load-bearing walls, is the quasi-static cyclic shear–compression test [27,29,43,44]. In this test, a constant vertical load and a cyclic horizontal displacement are applied to the specimen. The cyclic horizontal displacement follows a protocol that specifies the increase in displacement amplitude from one cycle to the next.

In an experimental campaign conducted at École Polytechnique Fédérale de Lausanne (EPFL), cyclic shear–compression tests on six full-scale plastered rubble stone masonry walls, labeled RS, were carried out [41]. These walls had a length, height and thickness of 1600 mm, 1600 mm and 400 mm, respectively (see Fig. 1a). They were built in two leaves with irregular limestone blocks, and the gap between the leaves was filled with pebbles and stone chips. A lime-based mortar—aggregate/binder ratio of 3/1—was used to fill the head and bed joints, where the binder was the commercially available OTTERBEIN natural hydraulic lime (NHL5). On every wall, the masonry was left visible on one side while the other side was plastered. Two consecutive layers of commercially available 'GeoCalce Intonaco' plaster were applied as illustrated in Fig. 1b, with the inner layer measuring about 4–6 cm thick and outer layer measuring 1 cm. The binder to sand weight ratio of 2/1 with 12 l of water was used in the first plaster layer. For the second layer, 25 kg of the binder was mixed with 5.1 l of water. Note that 1–2 cm at the top and bottom of the wall was left without plaster to ensure that the load was applied to the masonry and not to the plaster.

The shear–compression tests were performed in two phases:

1. In the first phase, we increased the forces F_{vn} and F_{vs} in the north and south vertical actuators (see Fig. 2) to apply a centric axial load N:

$$N = \frac{\sigma}{f_c} f_c L t, \tag{5}$$

where σ/f_c is the axial load ratio, which is defined as the ratio of the axial stress applied to the top of the wall to the compressive strength of the masonry, L is the length of the wall and t is its thickness.

2. In the second phase, we applied cyclic horizontal displacements of increasing drift demand through the horizontal actuator. During this phase, we operated the two vertical actuators to ensure a constant axial load and a constant shear span according to the equations:

$$F_{vn} = -\frac{N}{2} + \frac{F_h}{d_{act}}(H_1 - H_0), \tag{6}$$

$$F_{vs} = -\frac{N}{2} - \frac{F_h}{d_{act}}(H_1 - H_0), \tag{7}$$

where F_h is the force exerted by the horizontal actuator (actuator 1 in Fig. 2a), d_{act} represents the distance between the center lines of the two vertical actuators and was equal to 2400 mm in these tests, H_1 is the distance between the middle axis of the horizontal actuator and the top of the foundation, and H_0 is the distance between the bottom of the wall and the point where the bending moment was maintained zero during the tests.

This testing campaign was primarily designed to enrich the existing database in terms of the response of stone walls to shear–compression loading [45]. Of particular interest were the drift limit states of rubble stone masonry walls, which is the most irregular and weakest masonry typology (class A according to Vanin et al. [45]). Two quantities were varied between the specimens: the axial load ratio σ/f_c and the shear span ratio H_0/H (H is the height of the wall). The test matrix is summarized in Table 1. The data obtained from the shear–compression tests are made publicly available in a permanent repository: https://doi.org/10.5281/zenodo.5052675. For a more detailed explanation about the conducted experimental campaign, refer to Rezaie et al. [41].

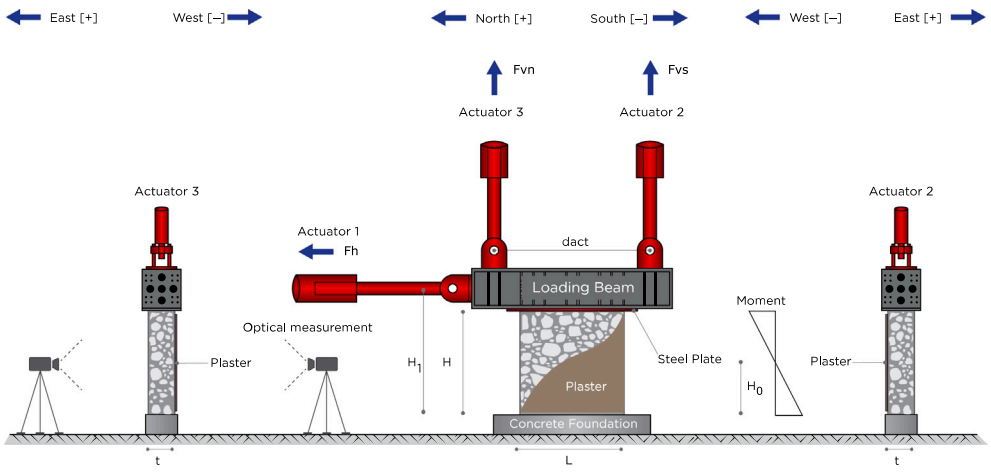

(a)

(b) (c)

Fig. 2. (a) Sketch of the test setup used for the cyclic shear–compression tests on six full-scale rubble stone masonry walls conducted by Rezaie et al. [41]; (b) view of the plastered side; (c) stone masonry side.

Table 1
Test matrix showing shear span and axial load ratio for the cyclic shear–compression tests on six full-scale rubble stone (RS) masonry walls conducted by Rezaie et al. [41].

Specimen label	σ/f_c	H_0/H
RS1	8%	0.5
RS2	25%	0.5
RS3	17%	0.5
RS4	25%	1.0
RS5	25%	1.5
RS6	17%	1.0

2.2. 3D DIC setup

In this campaign, stereo–camera systems (see Fig. 3) were used to capture gray-scale images from either sides of the walls during the entire loading sequence. These images were fed into a DIC method implemented in the commercial software VIC-3D version 8.2.4 [46], which computed the 3D deformation of the walls' plastered and masonry sides. The following preparation steps were required to use the DIC method and obtain reliable displacement field results:

1. Paint the walls' plastered and masonry sides in white.
2. Spray black speckle patterns (dots) with the average size of 2 mm on the walls' plastered and masonry sides (see Figs. 3a and 3b).
3. Provide proper lightning condition using LED lamps.
4. Calibrate cameras by taking pairs (around 80 pairs) of photos of a calibration board with circular dots of known dimension. We used the calibration algorithm implemented in the VIC-3D software [46] to obtain intrinsic and extrinsic camera parameters.

Acquired images were synchronized with the values of the vertical and horizontal forces applied to the specimens. Therefore, there are corresponding gray-scale images for each data point of the horizontal force–displacement response of the walls. As an illustration, Fig. 8 plots the horizontal force–drift response of specimen RS6 and provides images taken at two states A and B, where the horizontal force is almost zero. These images are 4384 × 6576 pixels in size, where each pixel corresponds to 0.43 mm (on average).

3. Detection and quantification of crack pattern

3.1. Crack segmentation

The process of using deep learning for crack detection and segmentation from images is a well-studied problem, and there are several articles addressing this using machine learning methods [42,47–52]. To detect surface cracks developed in the plastered side of the walls in this study, we used a deep convolutional neural network trained in our previous study for detecting crack pixels on laboratory images [42]. The trained encoder–decoder architecture is a variant of U-Net [53] and

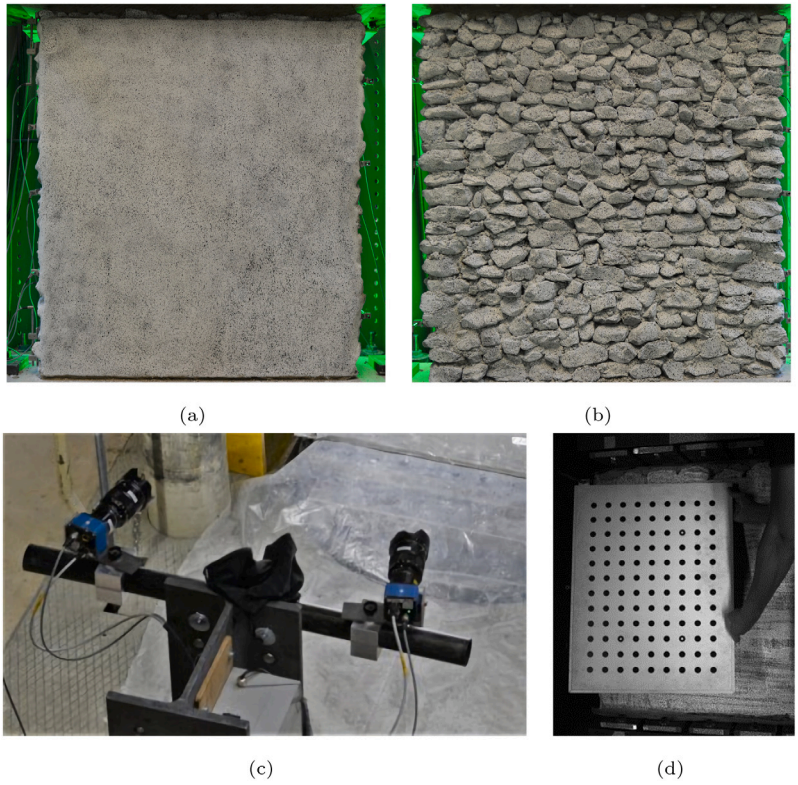

Fig. 3. View of speckled (a) plastered side and (b) masonry (stone) side of the specimens tested under cyclic shear–compression load by Rezaie et al. [41]; (c) stereo–camera system used to acquire pairs of gray-scale images; (d) calibration board used to calibrate cameras of the stereo-system.

includes a pre-trained VGG16 [54] on the ImageNet database [55] as an encoder. For a detailed analysis of the performance of the trained network in segmenting crack pixels, refer to Rezaie et al. [42]. An illustration of a gray-scale image taken from specimen RS5 at the drift value of 1.66% and the corresponding crack mask predicted by the trained deep model is shown in Fig. 4. It can be seen that the prediction made by the deep learning model [42] is pixel-wise, meaning that all pixels belonging to a crack are detected and represented as white pixels, while the others are represented as black pixels. Note that the prediction mask in this figure is cleaned to reflect only the area of interest, meaning that falsely detected crack pixels outside of the wall area were removed.

3.2. Crack cleaning and skeletonization

Errors are often present in deep-learning predictions used for crack detection; some cracks can be missed, and some pixels that do not belong to a crack can be misclassified as cracks. Here, we applied several post-processing steps to obtain a clean crack pattern and removed noisy results. These steps and the reasons for implementing them are outlined briefly in the following:

1. **Filling holes**: To compute the crack width from the DIC output, we first find the centerline of the cracks (see Section 3.3). To avoid branching of the centerlines, holes in the crack maps must be filled. This operation is detailed in Section 3.2.1.
2. **Skeletonization**: The centerlines are determined by applying a skeletonization algorithm to the detected crack pattern (see Section 3.2.2).
3. **Linking crack skeletons**: To preserve the continuation of crack centerline networks, centerlines close to each other are connected (see Section 3.2.3).
4. **Removing short crack branches**: The crack segmentation model falsely classifies some non-crack pixels as cracks [42]. These false positives appear as a small group of pixels. To remove these misclassified crack pixels, a threshold is applied to the area of the connected skeleton crack pixels (see Section 3.2.4).

All these steps were implemented in a Python code using the open-source image processing libraries scikit-image version 0.16.2 [56] and mahotas version 1.4.9 [57].

3.2.1. Filling holes

The crack pixels segmented by the deep model by Rezaie et al. [42] sometimes contain small holes that could negatively affect the skeletonization of crack patterns. To fill these gaps in the detected crack maps, a mathematical morphology operation called closing was applied [58] using a square structuring element of 10 × 10 pixels (4.3 × 4.3 mm^2). The size of the structuring element needs to be chosen on case-by-case basis. This filling operation was implemented using a scikit-image function called skimage.morphology.binary_closing, and an example image that has attained this process is shown in Fig. 5.

3.2.2. Skeletonization

Each detected crack branch was reduced to a single-pixel-wide skeleton using the function morphology.skeletonize from the scikit-image library. Fig. 6 illustrates this operation for an example image.

3.2.3. Linking crack skeletons

After extracting the crack skeletons, some crack branches were fragmented (see Fig. 7a). To connect these fragmented skeleton branches, the following steps were implemented: (a) find the distance transform of the inverse image (see Fig. 7b); (b) apply a threshold to the distance map; (c) skeletonize the threshold image from the previous step (see Fig. 7c).

(a) (b)

Fig. 4. Example of crack segmentation by the trained deep learning model developed by Rezaie et al. [42]. (a) The gray-scale image of specimen RS5 at the drift value of 1.66% used as the input to the deep model. The brightness of this image was changed for enhanced visualization. (b) The cleaned output of the deep model, which is a binary image where white pixels represent cracks and black pixels represent non-cracked areas of the wall. In this crack mask, the false-positive crack pixels that were outside the plaster area were removed.

(a) (b) (c)

Fig. 5. Illustration of the binary closing operation used to fill gaps in detected crack patterns. (a) An image patch sized 256 × 256 pixels was extracted from the original image; (b) the detected binary image of crack pixels with holes; (c) the result after binary closing was performed using a square structuring element of 10 × 10 pixels.

(a) (b) (c)

Fig. 6. Illustration of crack skeletonization. (a) An image patch of 256 × 256 pixels was extracted from the original image; (b) the detected binary image of crack pixels; (c) the crack skeleton.

3.2.4. Removing short crack branches

Using the function regionprops from the scikit-imag library, crack skeleton branches with areas smaller than a threshold of 30 pixels (~13 mm) were removed. Fig. 9 illustrates the detected crack skeleton formed via the reduction of binary crack maps to single-pixel wide objects after applying the aforementioned steps for the example image shown in Fig. 8b. Note that the crack detection and skeletonization were performed individually at a given time step irrespective of the previous or successive time step.

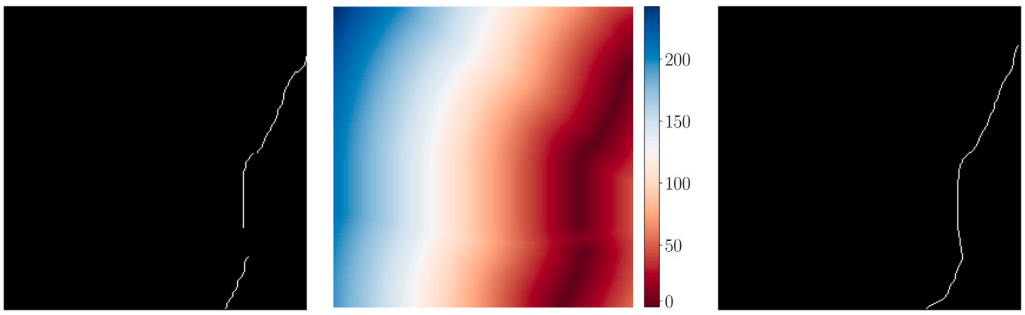

Fig. 7. Illustration of linking crack skeletons. (a) An image with fragmented crack skeletons; (b) distance transform of the inverse crack skeleton image; (c) the result after applying a threshold on the distance transform and then thinning.

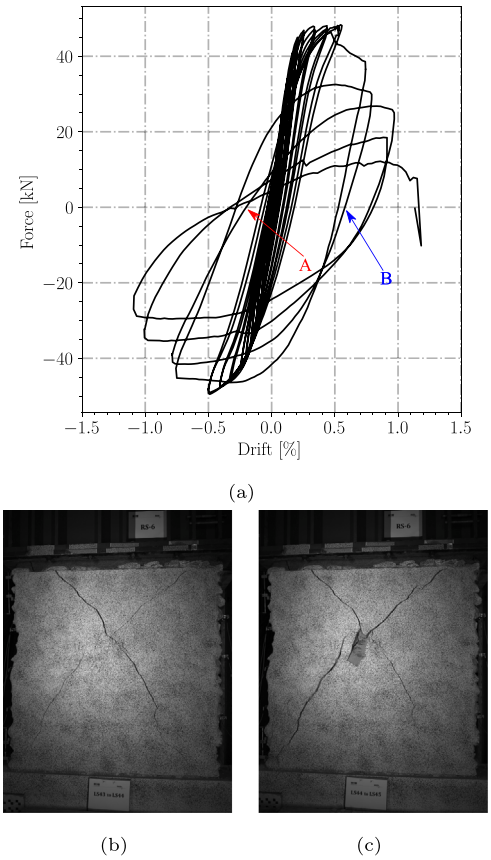

Fig. 8. (a) Horizontal force–drift response of specimen RS6 [41]; (b) the image taken at state A, corresponding to the data point where the horizontal force is almost 0 and the drift value is equal to −0.28%; (c) the image taken at state B, corresponding to the data point where the horizontal force is almost 0 and the drift value is equal to 0.57%. Both images shown here were taken by the stereo system's right camera located on the plastered side of the wall. The brightness of the images was adjusted and they were cropped for enhanced visualization.

3.3. Computation of crack width

The output of the DIC method is a 3-dimensional (3D) displacement field on a grid of points. We developed a Python code to compute the crack width by combining the segmented crack skeleton with the displacement field extracted from the VIC-3D software. Gehri et al. [59] have also recently developed a MATLAB-based software to compute crack kinematics from the outputs of the VIC-3D software. Ours differs in several aspects, including the detection of cracks, computation of crack orientation and width, and treatment of the outliers. The steps implemented in our code are summarized in the following:

1. **Computing crack skeleton pixel orientation**: For each crack skeleton pixel, the orientation with respect to the horizontal axis (axis c in Fig. 10) was computed. To do this, the center of a square kernel of 21 × 21 pixels, or 9 × 9 mm^2, (shown as k in Fig. 10) was placed at each crack skeleton pixel, and a line was fitted to the crack pixels present in the kernel (see Fig. 10). The slope of the line was considered to correspond to the local orientation of the crack skeleton pixel. The angle of crack pixels ranges between −90° and 90°, and is positive when rotating clockwise with respect to the horizontal axis.
2. **Reading horizontal and vertical displacement of two sides of the crack surface**: For each crack skeleton pixel, we obtained the horizontal and vertical displacement of two points placed 40 pixels (~17 mm) away from the crack pixel in the direction perpendicular to the orientation of the crack pixel (points A and B in Fig. 10). The displacements were obtained by interpolating the DIC outputs at the specified points of the image.
3. **Computing crack width**: Using the computed displacement vectors of two points at both sides of the crack surface and the orientation of crack pixels in previous steps, we projected the displacement vectors perpendicular (along the axis n in Fig. 10) and parallel (along the axis t in Fig. 10) to the crack surface. For each crack pixel, the component perpendicular to the crack surface is the crack width.
4. **Removing outliers**: The displacement field computed by the DIC can be noisy. As a result, the computed crack widths can be noisy. To remove such noisy results, the following two steps were implemented:
   (1) One output of the VIC-3D software is the sigma field (computed pixel-wise), which is the confidence bound in the match considered as the larger eigenvalue of the inverse of the Hessian matrix of the image [60]. Sigma values larger than 0 indicate noise. A user-defined upper-bound was set to discard the noisy displacement field of points A and B. This upper bound was not constant and varied between the analyzed images. It was selected based on engineering judgment, by checking whether the computed crack width was physically meaningful or not. In this study, an upper bound range of 0.03–0.05 pixels was used.
   (2) After the first step for outlier removal, there were still several cases with a computed maximum crack width that was too large and with no physical meaning. As a second step for removing outliers, we first computed the crack width directly from the crack masks segmented by the deep learning method. Here, the crack width was calculated as the number of crack pixels perpendicular to the crack orientation times the mm/pixel ratio. Then, we discarded the crack widths, which had a significant difference with respect to those obtained from the DIC outputs.

Table 2
Comparison of the crack width at certain locations on the plastered side of the walls measured by a crack gauge during the tests and computed by our code.

Index	Specimen label	Horizontal force [kN]	Drift [%]	Crack width [mm]	
				Crack gauge	Our code
1	RS3	−49.0	−0.20	2.50	2.87
2	RS3	−40.0	−0.31	1.00	1.10
3	RS4	−55.0	−0.15	0.50	0.48
4	RS4	−54.0	−0.15	0.60	0.66

Table 3
Values of maximum residual crack width after reaching the peak force and the ultimate drift in the quasi-static cyclic shear–compression tests performed by Rezaie et al. [41].

Specimen label	σ/f_c	H_0/H	Maximum residual crack width [mm][a]			
			Peak force		Ultimate drift	
			Flexure	Shear	Flexure	Shear
RS1	8%	0.5	0.1	0.9	0.2	2.1
RS2	25%	0.5	0	0.7	0	2.6
RS3	17%	0.5	0	1.3	0	3.8
RS4	25%	1.0	0	1.0	0	9.4
RS5	25%	1.5	0.7	0	[b]	[b]
RS6	17%	1.0	0.6	1.0	0.5	9.6
Mean ± standard deviation			0.5 ± 0.3	1.0 ± 0.2	0.4 ± 0.2	5.5 ± 3.3

[a]The values reported in this table are the average maximum crack width of the positive and negative residual drifts (first and third quadrant of the force–drift plots of Fig. 12).
[b]Since the specimen RS5 collapsed before reaching a 20% drop in force, the values for the ultimate drift limit are not reported.

The threshold used here also varied between images and could be adjusted by the user. A threshold range of 50–80 pixels was finally used.

To verify the adequacy of the chosen kernel size, 21 × 21 pixels (~9 × 9 mm^2), and the distance from the crack pixel, 40 pixels (~17 mm), we compared the crack width computed by our code with the manual measurement of crack width using a crack gauge at certain locations on the plaster. The crack gauge could measure a discrete set of crack widths of 0.10, 0.15, 0.20, 0.25, 0.30, 0.35, 0.40, 0.50, 0.60, 0.80, 1.00, 1.50, 2.00, 2.50 mm. From Table 2, it can be seen that the crack widths measured by the crack gauge and those obtained by our code are satisfactorily close.

To explore the sensitivity of the kernel size (k) and the distance to the crack pixel on the measured crack width, Fig. 11 plots the crack width measured by our code as a function of these two parameters. Regarding the distance to the crack (Fig. 11a), up to 40 pixels, the crack widths computed for all four examples seem to be constant. However, for distances larger than 40 pixels, the crack width computed for the example of index 1 starts to increase with the distance. It can also be seen from Fig. 11b that the measured crack width is not sensitive to the kernel size for the examined range. In conclusion, the comparison between the crack width measured by the crack gauge during the test and the one computed by our code justifies the chosen kernel size of 21 × 21 pixels and the distance to the crack of 40 pixels.

4. Relationship between crack width and drift

4.1. Crack width at drift demand and residual drift

Fig. 12 illustrates the force–drift diagrams of the tested walls along with the damage patterns developed right before the loss of the axial load-bearing capacity of the walls. In general, the cracks developed in this test series can be categorized into two types: (a) shear cracks, i.e. diagonal cracks which appear in the middle of the specimens and progressively spread towards the wall corners; (b) flexural cracks, i.e. horizontal cracks forming mainly at the toes of the specimens or at the wall/foundation interfaces. For a more detailed explanation of each specimen's failure sequence, refer to Rezaie et al. [41].

Fig. 13 plots the maximum crack width as a function of the maximum drift demand reached during each cycle. The red and blue markers represent, respectively, the maximum crack width at the maximum drift and residual drift, the latter indicating the unloading from the maximum-drift state to the zero-force state. The black, orange, and green dashed lines indicate respectively the drifts at peak force, ultimate, and collapse drift limits resulting from the tests [41]. Note that in the last cycles of the loading protocol, those with the highest drift demands, the plaster detached from the specimens and the cracking was considerable; since the DIC results were not reliable in those cases, the corresponding maximum crack width values are not reported in Fig. 13.

Flexural and shear cracks can be easily distinguished in Fig. 13, in relation to the development of the crack width and crack opening/closing sequence:

1. **Flexural cracks**: Examples of flexural cracks were observed at the wall/foundation interface of specimens RS5 and RS6 [41]. The plots related to these cracks (see Fig. 13e and f) show that, up to a drift smaller than the one reached at the peak force, the maximum crack width increases with the drift demand but drops almost to zero when the specimen is unloaded, i.e. the flexural cracks open when loading and close upon load removal.
2. **Shear cracks**: Examples of shear cracks were observed in the middle of specimens RS2 and RS3 [41]. The opening/closing sequence followed by these cracks (see Fig. 13b and c) is visibly different compared to the one of the flexural cracks. In fact, the maximum crack width at the residual drift is, for the majority of the drift demands, close to the crack width attained at the maximum drift. In other words, the maximum crack width does not change significantly when unloading the specimen. This results in hysteresis loops with near-vertical unloading branches and higher energy dissipation, as compared to those of the walls developing flexural cracks (see Fig. 12).

4.2. Residual crack width at peak force and ultimate drift

Table 3 gives the maximum crack width obtained at the residual drift attained at the peak force and ultimate drift. For both drift limits, the average residual width of the flexural cracks developing at the wall/foundation interface is relatively small and ranges between 0.4–0.5 mm. This is expected, as the flexural cracks tend to close after unloading (Fig. 13). However, for the shear cracks the difference is significant. The average maximum residual crack width is 1.0 mm at the peak force and 5.5 mm at the ultimate drift.

4.3. Residual shear crack width as a function of shear span and axial load ratio

Fig. 14 plots the maximum residual shear crack width as a function of the shear span and axial load ratio, for both the peak force and ultimate drift limits. In general, there is no clear trend between the axial load ratio and the residual shear crack width (Fig. 14). A trend can be observed at the ultimate drift, where the residual shear crack width appears to be larger for walls with higher shear span ratio (Fig. 14b). In particular, for specimens with the shear span ratio of 0.5 (walls RS1, RS2, and RS3) the average residual shear crack width is about 2.8 mm, while for specimens with shear span ratio of 1.0 (walls RS4 and RS6) a value of almost 9.5 mm is obtained.

The reason for such a dependency on the shear span ratio can be searched in the experimental results, which showed that the walls with a higher shear span ratio display a larger displacement capacity (see Fig. 12). Here, it is also observed that, especially in the post-peak regime, the measured deformation tends to concentrate along previously formed diagonal cracks rather than forming new cracks,

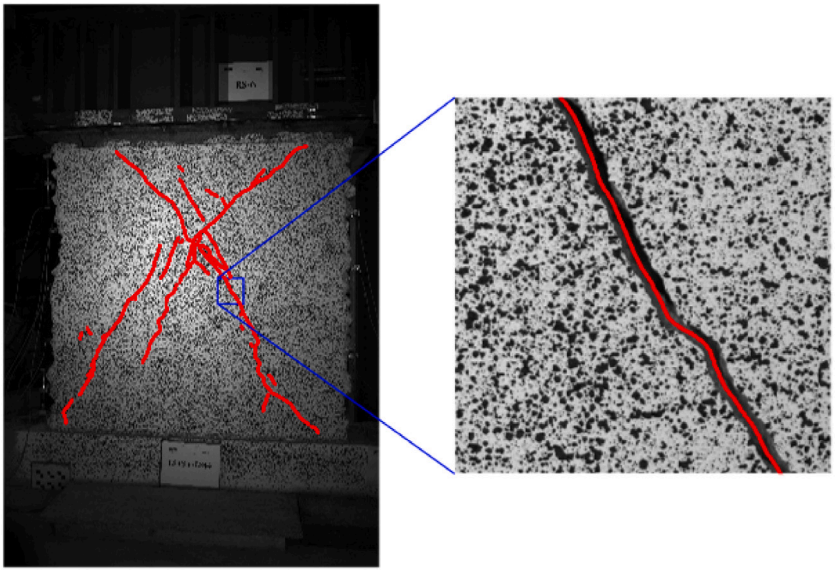

Fig. 9. Illustration of the detected crack centerlines for the example image shown in Fig. 8b. The crack centerlines (skeletons) are highlighted in red.

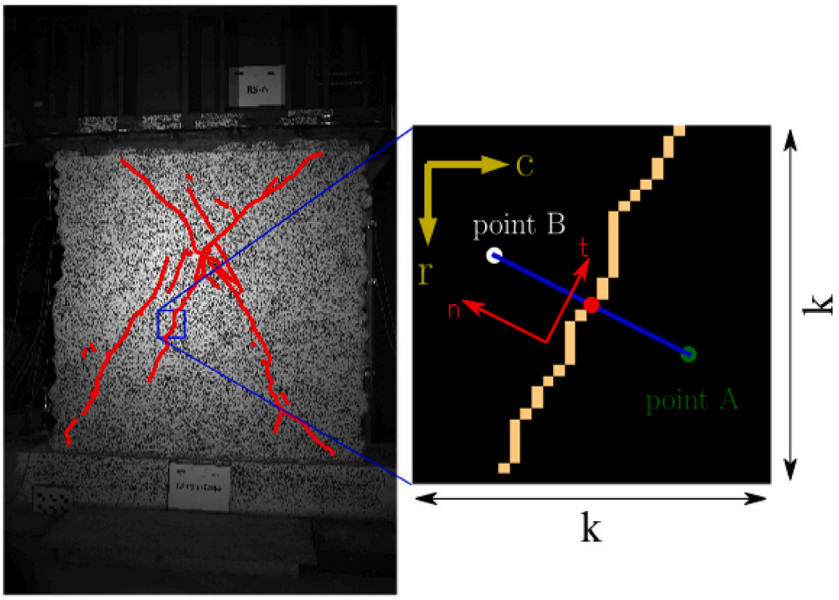

Fig. 10. Illustration of the computation of the crack pixel orientation and the coordinates of the points A and B. Here, the crack pixel of interest is highlighted in red, k is the size of the kernel in terms of pixel, and c and r are the local coordinate system in the kernel.

which manifests as an increase in the width of the diagonal cracks. As an illustration, Fig. 15 shows the crack pattern and concentration of deformation obtained by our code along the diagonal cracks of specimen RS4 at two instances of the force–drift diagram. To illustrate the concentration of deformation on the wall surface, the thickness of the crack skeleton was made proportional to the measured crack width.

4.4. Dependency of shear crack width on loading protocol

In the conducted testing campaign [41], the horizontal displacement was applied according to a loading protocol that increased the drift demand levels after performing two cycles per drift level. Classically, two or three cycles per drift demand are applied during shear–compression tests. Few studies explored the effect of the loading protocol on the force–drift behavior of the walls [29,61], this aspect being usually limited to the difference between monotonic and cyclic loading, and not the number of applied cycles.

To illustrate the influence of the loading protocol on the development of cracking, Fig. 16 shows, for each cycle, the maximum shear crack width at the states of maximum force (the one ever reached during each cycle) and residual drift, for two selected points of the crack skeleton of specimen RS3. These two points were selected because they belong to cracks propagating in two opposite directions (45° and −45°). It can be seen that, upon repetition of the drift demand, the maximum shear crack width becomes higher, both when reaching the maximum force and at the residual drift. This means that damage accumulates when the wall is loaded to the same level of drift for the second time.

In order to rationalize this and better illustrate the kinematics of the wall, displacement vector fields of specimen RS3 are shown in Fig. 17 for different force–drift combinations. These combinations include the following states: (i) when the beam is at its original position (drift = 0.0%); (ii) when the maximum force is reached in a given cycle, and (iii) when the force is almost zero (residual drift). Fig. 17a

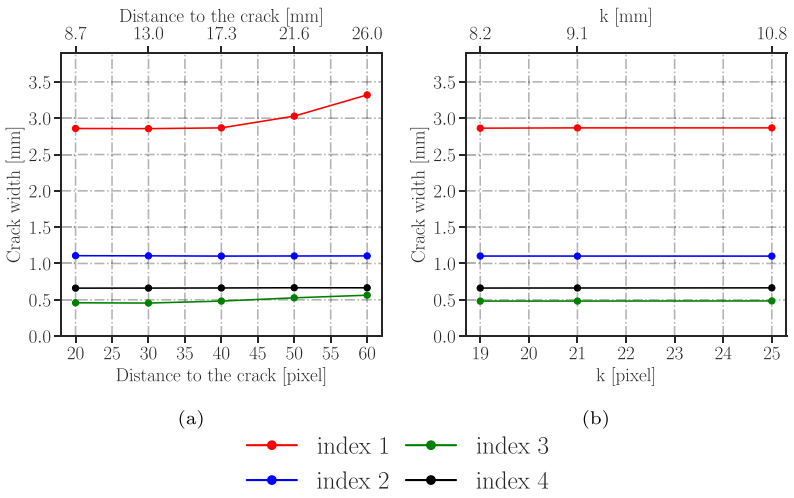

Fig. 11. Plots of crack width as a function of (a) distance to the crack pixel and (b) kernel size (k) for all examples in Table 2.

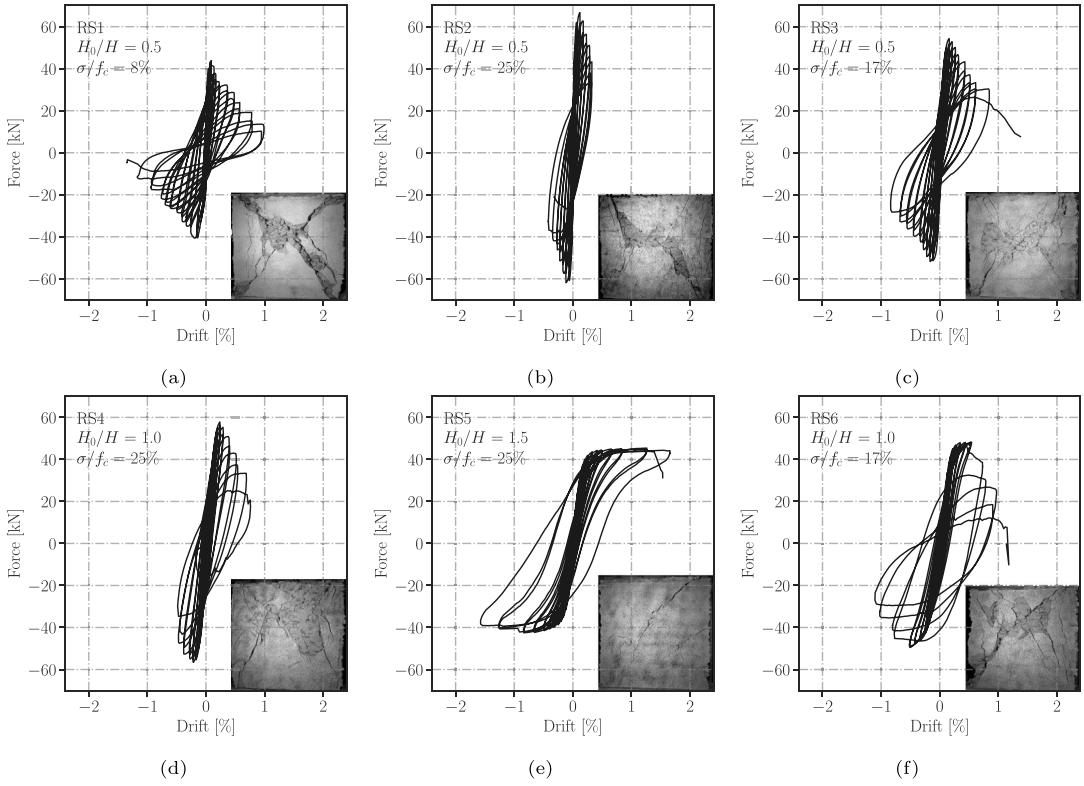

Fig. 12. Plots of the force–drift response and the crack pattern obtained before the loss of the axial load-bearing capacity [41].

clarifies that the wall was divided into four semi-rigid blocks consisting of top/bottom triangles and left/right quadrilaterals at this state. It appears that when the wall is loaded in the positive or negative direction (see Figs. 17b, 17d, and 17g), the blocks above the formed diagonal cracks move with the beam while the bottom triangle remains in its original position. This also illustrates that, when the beam is at its original position (drift = 0.0%), there is a considerable residual displacement in the left/right quadrilaterals, which is why the crack width becomes higher in the second cycle.

To better highlight the residual displacement of the two lateral blocks, Fig. 18 plots the difference between the displacement vector fields shown in Figs. 17a–f and 17b–g. Each color used in this plot represents a vector in the color code shown in Fig. 18c. The white color represents the zero displacement vector $\vec{0}$.

Finally, to quantify how the distribution of the residual crack widths changes within the crack patterns between two consecutive cycles, Fig. 19 provides the box plots of this quantity at the first and second cycles, and for various residual drift levels. Visibly, for all specimens and reported drift levels, the application of the second cycle has a relatively important effect on the crack width distributions. To be more specific, the box plots corresponding to the second application of the drift demand (in orange in Fig. 19) became longer than the ones related to the first cycle (in blue in Fig. 19). In other words, the range of the crack widths – defined as the delta between maximum and minimum crack widths – increased in the second cycle (in orange in Fig. 19) compared to the first cycle (in blue in Fig. 19). Additionally, the same increase was observed in the 75th percentile (upper quartile) of the distribution of the crack widths in the second cycle. But, with regard to the median, no consistent trend was noticed.

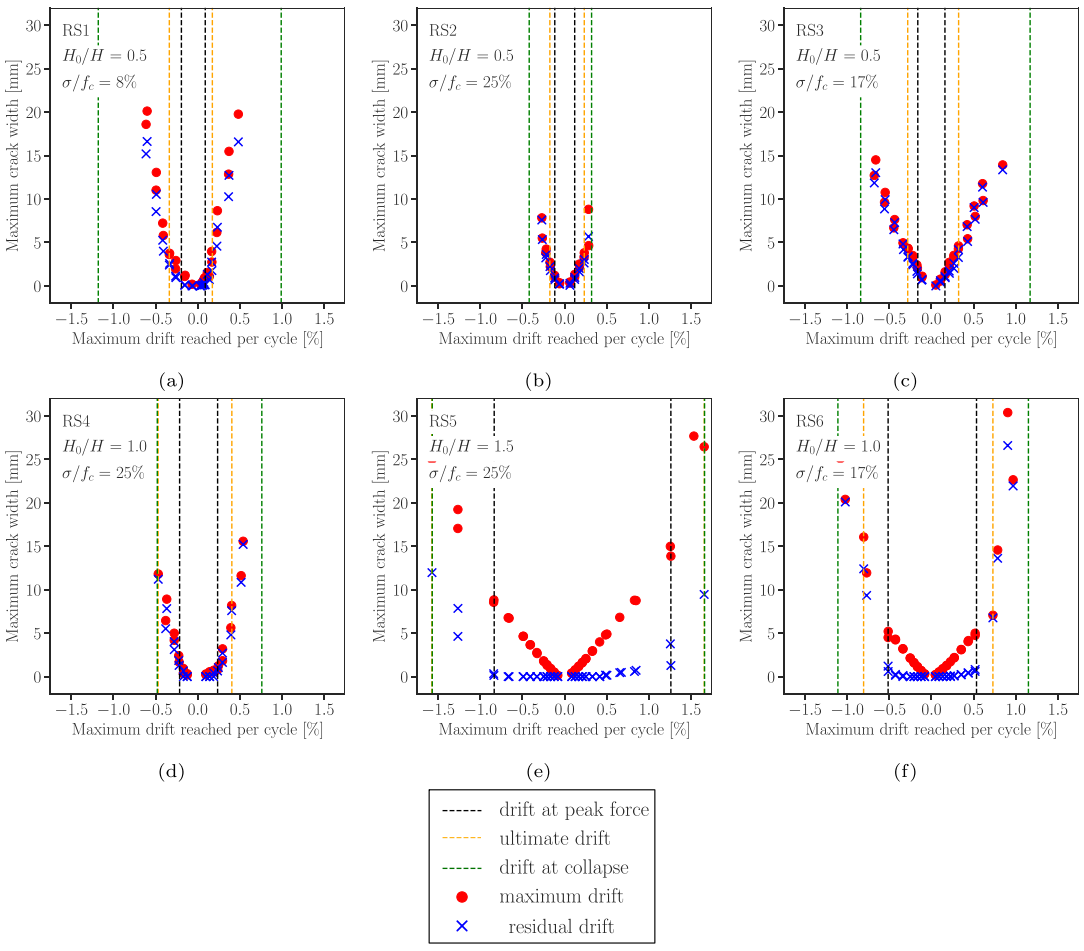

Fig. 13. Plots of maximum crack width versus maximum drift reached per cycle of the stone masonry specimens tested under quasi-static cyclic shear–compression by Rezaie et al. [41]. (For interpretation of the references to color in this figure legend, the reader is referred to the web version of this article.)

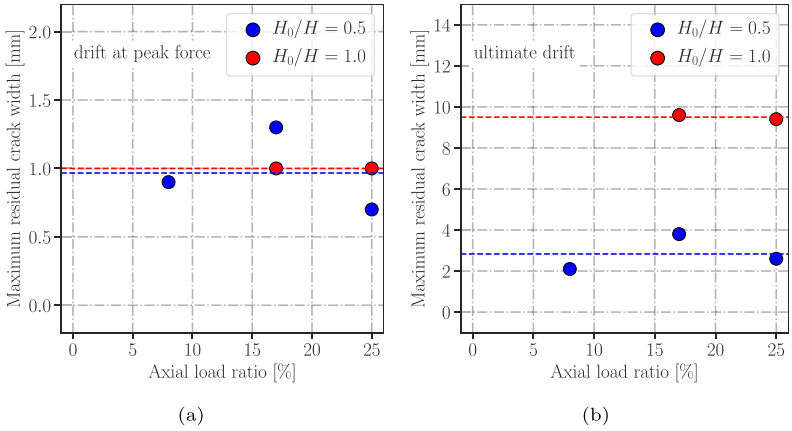

Fig. 14. Plots of residual shear crack width as a function of the axial load and the shear span ratio. The dotted lines represent the average values.

5. Conclusion

Maximum crack width is used in the literature to express the level of damage due to a cyclic shear–compression load applied to a masonry pier. In this study, we further investigated: (a) the influence of several parameters affecting the maximum crack width, including the shear span ratio, the axial load ratio, the type of crack, and the loading protocol; and (b) how the maximum crack width changes from the applied drift demand to the residual drift.

To address these topics, we used data from an experimental campaign employing quasi-static cyclic shear–compression tests on six full-scale rubble stone masonry walls conducted at École Polytechnique Fédérale de Lausanne (EPFL) [41]. One side of each wall was covered with plaster while the other one was left bare. Two stereo–camera systems were used to record gray-scale images of the surface of the specimens during the application of the load. These images were used as input for the DIC method to compute the displacement field as well as for the deep model previously developed by the authors [42] to detect crack pixels.

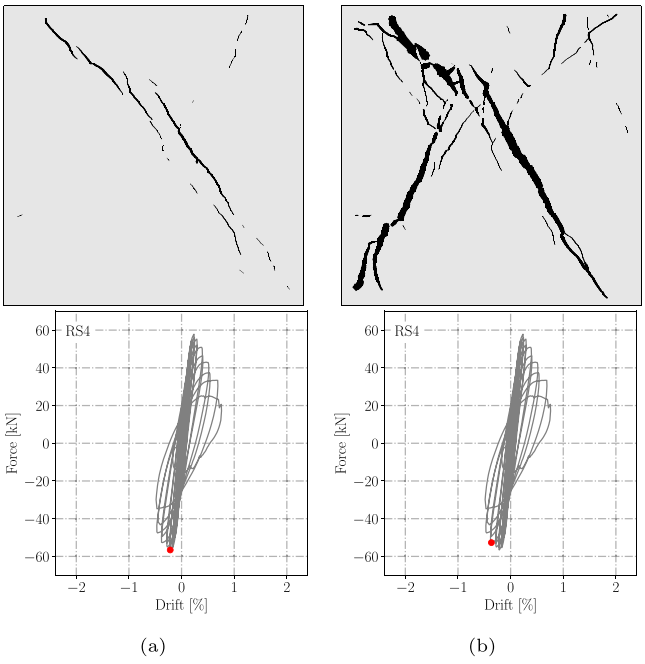

Fig. 15. Crack pattern and concentration of deformation along the diagonal cracks of specimen RS4 at two instances: (a) drift = −0.22%, force = −56.6 kN; (b) drift = −0.36%, force = −52.7 kN. To illustrate the concentration of deformation, the thickness of the crack skeleton is made proportional to the measured crack width.

A series of Python codes was developed to: (a) post-process the crack masks outputted by the deep model, including filling gaps, skeletonization, linking crack skeletons, and removing small cracks; and (b) compute the crack width for each crack skeleton pixel from the DIC outputs. To determine the orientation of the crack skeleton pixels, we verified the choice of the kernel size by a sensitivity analysis. We also verified the distance to the crack pixel, which is used to obtain the displacements of the points on two sides of the crack fronts, by comparing the crack width computed from the DIC outputs with the values recorded using a crack gauge during the test survey. The codes were used to automatically compute crack width at the instance of residual drift, maximum force, and maximum drift demand per cycle and to investigate a number of factors on the crack width values.

The following summarizes the main findings:

- Two types of cracks developed in the tested walls: flexural and shear. It was shown that, when moving from the applied drift demand to the residual drift, the maximum diagonal shear crack width did not reduce significantly, while the flexural cracks tended to close. This finding has practical implications on post-earthquake assessments: (i) For diagonal shear cracks, the residual crack width measurements after an earthquake can approximate the crack width at the peak displacement demand. Conversely, if experimental campaigns only report crack widths at peak drift, these values can be used to assess limit states after earthquakes. (ii) Some documents (e.g. AeDES [24] and FEMA 306 [2]) do not indicate whether the reported diagonal crack widths in masonry walls are at peak or residual. Our results suggest that this missing information does not compromise the application of the document.
- No clear trend could be observed between the axial load and shear span ratio and the maximum residual crack width at the peak force limit state. However, at the ultimate drift limit state, the maximum residual crack width obtained in walls with a shear span ratio of 1.0 was significantly higher than walls with a shear span ratio of 0.5. We argued that the higher drift capacity of the cantilevered walls and the concentration of deformation along the diagonal cracks are the reasons for obtaining higher residual crack width for walls with a shear span ratio of 1.0.
- The crack width increased in specimens loaded to the same level of drift for the second time, which shows the dependency of crack width on the loading protocol. Plotting the displacement vector fields revealed that the selected specimen (RS3) was divided into four semi-rigid blocks, top/bottom triangles and left/right quadrilaterals. The bottom triangle remained in its original position during the loading sequence, while the top triangle moved with the loading beam. The residual displacement of the left and right quadrilaterals was considered to be the main reason for the increase in crack width in the second cycle when the same level of drift was reached for the walls with diagonal shear cracks. Additionally, the increase in crack width in the second cycle was shown using box plots of residual crack width at two consecutive cycles. The maximum crack width and the 75th percentile were higher in the second cycle compared to the first.

In this study, the crack detection was conducted individually for each image without considering the previous or the next recorded images. In future studies, incorporating time could improve the detection of crack pixels. Additionally, other features such as the fractal dimension, density of cracks, length, complexity dimension, etc. can be used to quantify crack patterns and correlate them with the degradation of force, drift capacity, and stiffness of the wall. This information can be used to improve automated post-earthquake assessments.

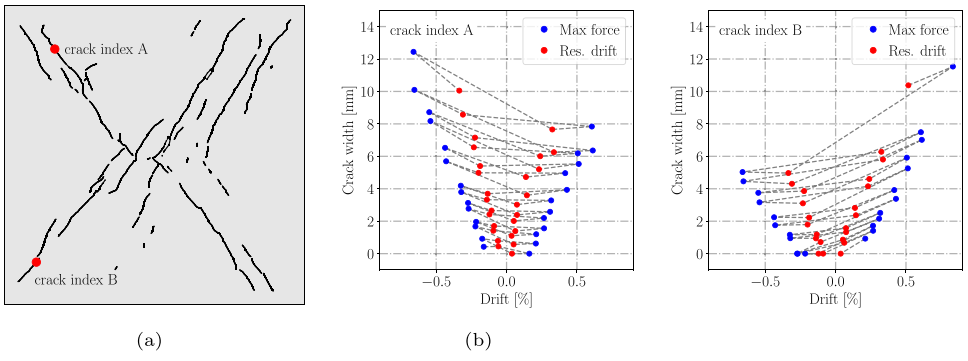

Fig. 16. Influence of loading protocol on the maximum shear crack width. (a) Illustration of crack pattern obtained for specimen RS3. (b) Plots of maximum shear crack width as a function of the drift at maximum force and residual drift, for crack index A and B.

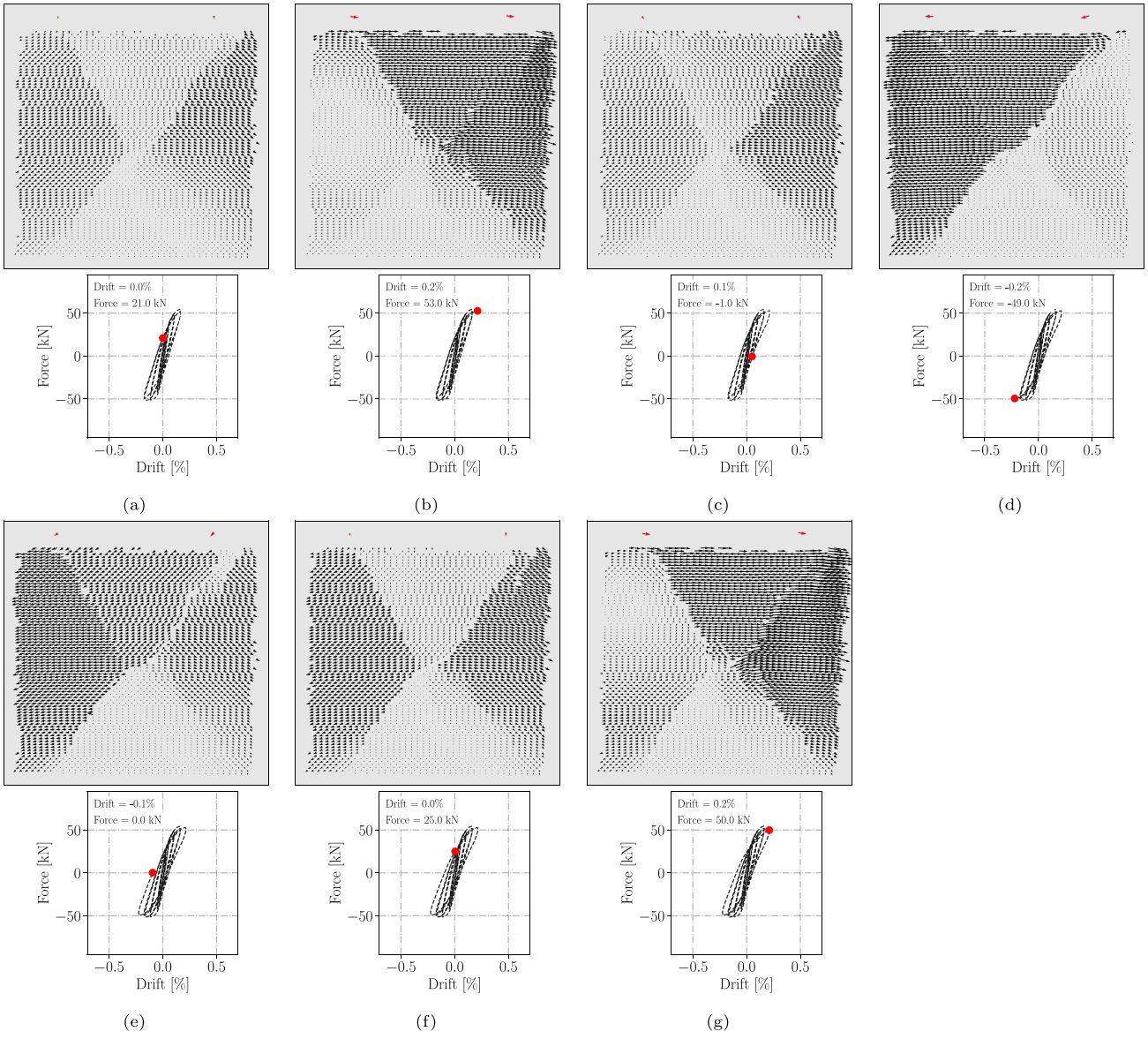

Fig. 17. Displacement vector field analysis of specimen RS3 at various force–drift combinations: (a) 0.0%, 21 kN; (b) 0.2%, 53.0 kN; (c) 0.1%, -1 kN (almost zero); (d) −0.2%, −49.0 kN; (e) −0.1%, 0.0 kN; (f) 0.0%, 25.0 kN; and (g) 0.2%, 50.0 kN. The reference configuration is the undeformed state of the wall before the application of the vertical force. The red arrows show the displacement vectors of the loading beam. The displacement vector plots have been flipped horizontally to align the loading direction with the positive direction of the drift coordinate axis in the force–drift plots.

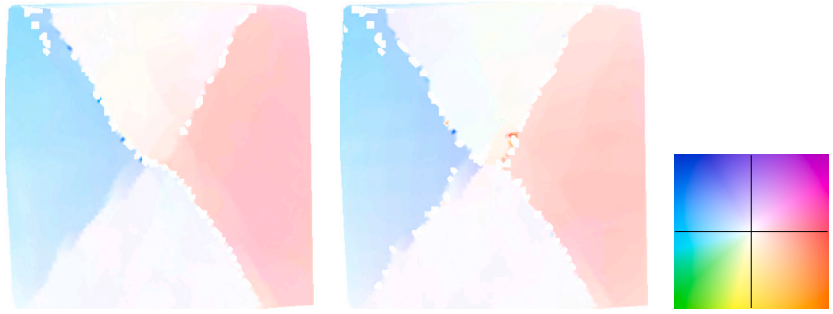

Fig. 18. Plot of the difference between the displacement vector fields shown in: (a) Figs. 17f and 17a; (b) Figs. 17g and 17b. (c) The displacement vector color code. (For interpretation of the references to color in this figure legend, the reader is referred to the web version of this article.)

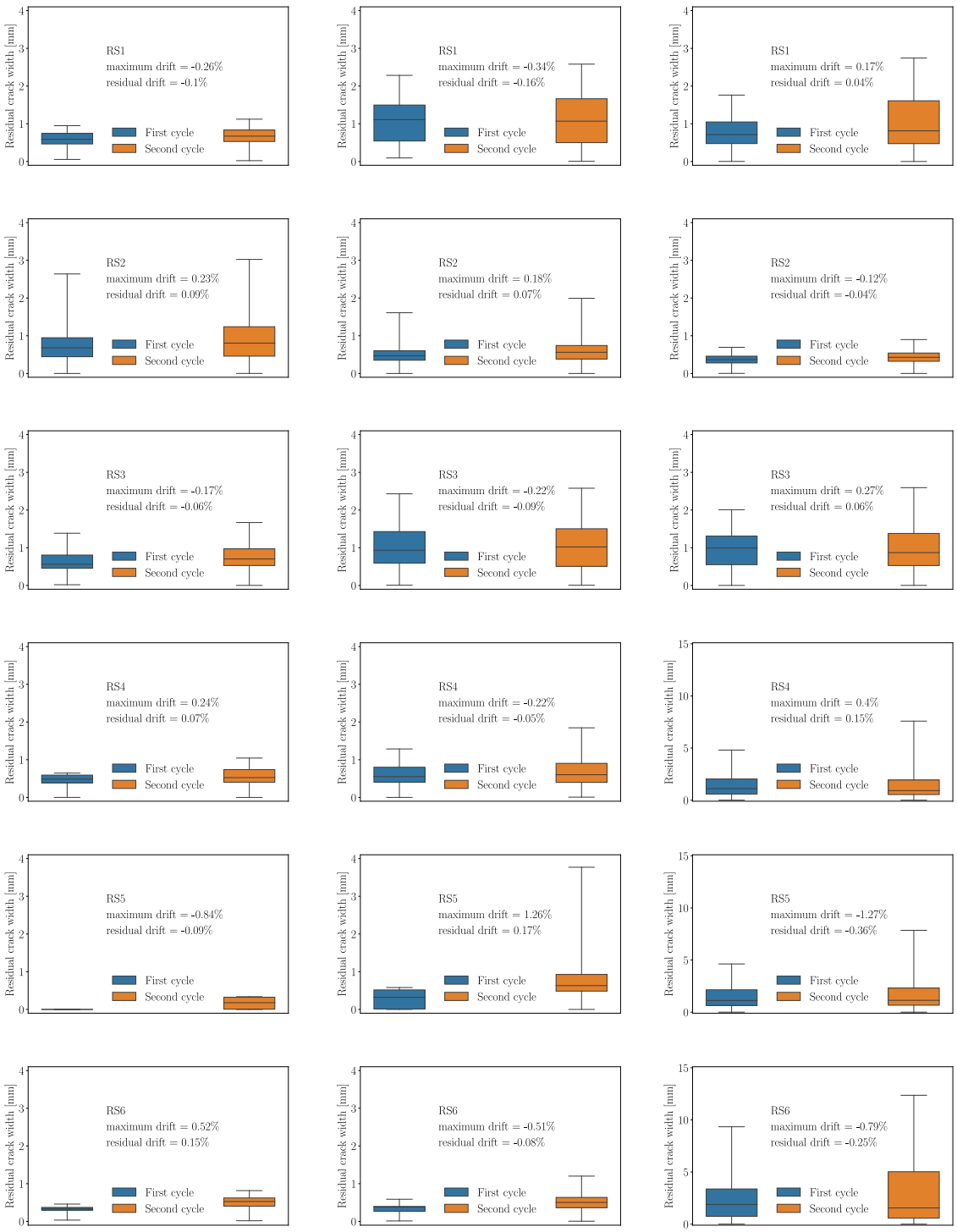

Fig. 19. Box plots of the residual crack width distributions at two consecutive cycles. The plots are reported for all tested walls at different drift levels. (For interpretation of the references to color in this figure legend, the reader is referred to the web version of this article.)

CRediT authorship contribution statement

Amir Rezaie: Methodology, Validation, Formal analysis, Investigation, Data curation, Writing - original draft, Writing - review & editing, Visualization. **Michele Godio:** Methodology, Investigation, Writing - original draft, Writing - review & editing, Visualization, Supervision. **Katrin Beyer:** Conceptualization, Methodology, Investigation, Resources, Writing - original draft, Writing - review & editing, Supervision, Project administration, Funding acquisition.

Declaration of competing interest

The authors declare that they have no known competing financial interests or personal relationships that could have appeared to influence the work reported in this paper.

Acknowledgments

This project is supported by the Swiss National Science Foundation (grant 200021_175903/1 "Equivalent frame models for the in-plane and out-of-plane response of unreinforced masonry buildings").

References

[1] D.F. D'Ayala, S. Paganoni, Assessment and analysis of damage in L'Aquila historic city centre after 6th april 2009, Bull. Earthq. Eng. 9 (2011) 81–104, http://dx.doi.org/10.1007/s10518-010-9224-4.
[2] FEMA 306, Federal emergency management agency, evaluation of earthquake damaged concrete and masonry buildings, 1998, URL: https://www.fema.gov/media-library/assets/documents/3068.
[3] R. Napolitano, B. Glisic, Hybrid physics-based modeling and data-driven method for diagnostics of masonry structures, Comput.-Aided Civ. Infrastruct. Eng. 35 (2020) 483–494.
[4] R. Napolitano, B. Glisic, Methodology for diagnosing crack patterns in masonry structures using photogrammetry and distinct element modeling, Eng. Struct. 181 (2019) 519–528.
[5] I.A.E. De Vent, J.G. Rots, R. van Hees, Structural Damage in Masonry: Developing Diagnostic Decision Support (Ph.D. thesis), TU Delft, Delft, 2011.
[6] K.M. Dolatshahi, K. Beyer, Stiffness and strength estimation of damaged unreinforced masonry walls using crack pattern, J. Earthq. Eng. (2019) 1–20, http://dx.doi.org/10.1080/13632469.2019.1693446.
[7] H.M. Madani, K.M. Dolatshahi, Strength and stiffness estimation of damaged reinforced concrete shear walls using crack patterns, Struct. Control Health Monit. 27 (2020) e2494, http://dx.doi.org/10.1002/stc.2494.
[8] Jonathan P. Rivera, Emma Lejeune, Bismarck N. Luna, Andrew S. Whittaker, Automated detection and measurement of cracks in reinforced concrete components, ACI Struct. J. 112 (2015) http://dx.doi.org/10.14359/51687424.
[9] M. Tomaževič, Damage as a measure for earthquake-resistant design of masonry structures: Slovenian experience, Can. J. Civil Eng. 34 (2007) 1403–1412, http://dx.doi.org/10.1139/L07-128.
[10] V. Bosiljkov, A.W. Page, V. Bokan-Bosiljkov, R. Žarnić, Evaluation of the seismic performance of brick masonry walls, Struct. Control Health Monit. 17 (2010) 100–118, http://dx.doi.org/10.1002/stc.299, URL: https://onlinelibrary.wiley.com/doi/abs/10.1002/stc.299.
[11] M. Kržan, S. Gostič, S. Cattari, V. Bosiljkov, Acquiring reference parameters of masonry for the structural performance analysis of historical buildings, Bull. Earthq. Eng. 13 (2015) 203–236, http://dx.doi.org/10.1007/s10518-014-9686-x.
[12] P.A. Korswagen, M. Longo, J.G. Rots, High-resolution monitoring of the initial development of cracks in experimental masonry shear walls and their reproduction in finite element models, Eng. Struct. 211 (2020) 110365, http://dx.doi.org/10.1016/j.engstruct.2020.110365, URL: http://www.sciencedirect.com/science/article/pii/S0141029619332341.
[13] D. Rouzbeh, M.G. R., K.J. Nathan, Structural load estimation using machine vision and surface crack patterns for shear-critical RC beams and slabs, J. Comput. Civ. Eng. 32 (2018) 4018024, http://dx.doi.org/10.1061/(ASCE)CP.1943-5487.0000766.
[14] J. P. Rivera, A. S. Whittaker, Damage and peak shear strength of low-aspect-ratio reinforced concrete shear walls, J. Struct. Eng. 145 (2019) 4019141, http://dx.doi.org/10.1061/(ASCE)ST.1943-541X.0002364.
[15] G. Abbiati, M. Broccardo, M. Didier, K. Beyer, B. Stojadinovic, A probabilistic damage model for predicting plaster cracks on unreinforced masonry walls, in: 16th European Conference on Earthquake Engineering, ECEE 2018, 2018.
[16] P.A. Korswagen, M. Longo, E. Meulman, J.G. Rots, Crack initiation and propagation in unreinforced masonry specimens subjected to repeated in-plane loading during light damage, Bull. Earthq. Eng. 17 (2019) 4651–4687, http://dx.doi.org/10.1007/s10518-018-00553-5.
[17] P.A. Korswagen, M. Longo, J.G. Rots, Calcium silicate against clay brick masonry: An experimental comparison of the in-plane behaviour during light damage, Bull. Earthq. Eng. 18 (2020) 2759–2781, http://dx.doi.org/10.1007/s10518-020-00803-5.
[18] A. Rezaie, A.J.P. Mauron, K. Beyer, Sensitivity analysis of fractal dimensions of crack maps on concrete and masonry walls, Autom. Constr. 117 (2020) http://dx.doi.org/10.1016/j.autcon.2020.103258.
[19] A. Ebrahimkhanlou, A. Farhidzadeh, S. Salamone, Multifractal analysis of crack patterns in reinforced concrete shear walls, Struct. Health Monit. 15 (2016) 81–92, http://dx.doi.org/10.1177/1475921715624502.
[20] A. Farhidzadeh, E. Dehghan-Niri, A. Moustafa, S. Salamone, A. Whittaker, Damage assessment of reinforced concrete structures using fractal analysis of residual crack patterns, Exp. Mech. 53 (2013) 1607–1619, http://dx.doi.org/10.1007/s11340-013-9769-7.
[21] H. Momeni, K.M. Dolatshahi, Predictive equations for drift ratio and damage assessment of RC shear walls using surface crack patterns, Eng. Struct. 190 (2019) 410–421, http://dx.doi.org/10.1016/j.engstruct.2019.04.018, URL: http://www.sciencedirect.com/science/article/pii/S014102961832697X.
[22] E. Arvin, A. Apostolos, H.T. D., B. Oguzhan, S. Salvatore, Fractal and multifractal analysis of crack patterns in prestressed concrete girders, J. Bridge Eng. 24 (2019) 4019059, http://dx.doi.org/10.1061/(ASCE)BE.1943-5592.0001427.
[23] J. Carrillo, W. Avila, Assessment of seismic damage of thin and lightly reinforced concrete walls using fractal dimension of cracking, Earthq. Eng. Struct. Dyn. 46 (2017) 661–675, http://dx.doi.org/10.1002/eqe.2808.
[24] C. Baggio, A. Bernardini, R. Colozza, L. Corazza, M. Della Bella, G. Di Pasquale, M. Dolce, A. Goretti, A. Martinelli, G. Orsini, Field Manual for Post-Earthquake Damage and Safety Assessment and Short Term Countermeasures (AeDES), European Commission—Joint Research Centre—Institute for the Protection and Security of the Citizen, 2007, EUR, 22868.
[25] V.I. Novelli, D. D'Ayala, Use of the knowledge-based system LOG-IDEAH to assess failure modes of masonry buildings, damaged by L'Aquila earthquake in 2009, in: Frontiers in Built Environment, vol. 5, 2019, p. 95, URL: https://www.frontiersin.org/article/10.3389/fbuil.2019.00095.
[26] G. Grünthal, European Macroseismic Scale 1998, European Seismological Commission (ESC), 1998.
[27] S. Petry, K. Beyer, Cyclic test data of six unreinforced masonry walls with different boundary conditions, Earthq. Spectra 31 (2015) 2459–2484.
[28] C. Calderini, S.D. Abbati, P. Cotič, M. Kržan, V. Bosiljkov, In-plane shear tests on masonry panels with plaster: Correlation of structural damage and damage on artistic assets, Bull. Earthq. Eng. 13 (2015) 237–256, http://dx.doi.org/10.1007/s10518-014-9632-y.
[29] M. Godio, F. Vanin, S. Zhang, K. Beyer, Quasi-static shear–compression tests on stone masonry walls with plaster: Influence of load history and axial load ratio, Eng. Struct. 192 (2019) 264–278, http://dx.doi.org/10.1016/j.engstruct.2019.04.041.
[30] M. Didier, G. Abbiati, F. Hefti, M. Broccardo, B. Stojadinovic, Damage quantification in plastered unreinforced masonry walls using digital image correlation, in: 10th Australasian Masonry Conference, 2018, pp. 14–18.
[31] G. Abbiati, M. Broccardo, A. Gabbi, N. Mojsilović, M. Petrović, B. Stojadinović, Calibration of a probabilistic fatigue model for predicting plaster cracks on unreinforced masonry walls caused by induced seismic hazard, in: Integrating Science, Engineering, & Policy: 11th National Conference on Earthquake Engineering 2018, 11NCEE, vol. 4, Curran Associates, 2018, pp. 2438–2448.
[32] X. Xie, L. Zhang, Z. Qu, A critical review of methods for determining the damage states for the in-plane fragility of masonry infill walls, J. Earthq. Eng. (2020) 1–22, http://dx.doi.org/10.1080/13632469.2020.1835749.
[33] Eurocode 8 - Part 3, Design of Structures for Earthquake Resistance-Part 3: Assessment and Retrofitting of Buildings, EN 1998-3, Technical Report Brussels, European Committee for Standardization, 2005.
[34] E. Vintzileou, I. Tselios, D. Karagiannaki, Quantification of damage to masonry structures under seismic conditions, in: Brick and Block Masonry-from Historical to Sustainable Masonry: Proceedings of the 17th International Brick/Block Masonry Conference, 17thIB2MaC 2020, July 5–8, 2020, Kraków, Poland, CRC Press, 2020, p. 451.
[35] S. Petry, K. Beyer, Influence of boundary conditions and size effect on the drift capacity of URM walls, Eng. Struct. 65 (2014) 76–88, http://dx.doi.org/10.1016/j.engstruct.2014.01.048, URL: http://www.sciencedirect.com/science/article/pii/S0141029614000625.
[36] S. Zhang, K. Beyer, Numerical investigation of the role of masonry typology on shear strength, Eng. Struct. 192 (2019) 86–102, http://dx.doi.org/10.1016/j.engstruct.2019.04.026, URL: https://www.sciencedirect.com/science/article/pii/S0141029618321515.
[37] S. Zhang, S.M. Taheri Mousavi, N. Richart, J.-F. Molinari, K. Beyer, Micromechanical finite element modeling of diagonal compression test for historical stone masonry structure, Int. J. Solids Struct. 112 (2017) 122–132, http://dx.doi.org/10.1016/j.ijsolstr.2017.02.014, URL: https://www.sciencedirect.com/science/article/pii/S0020768317300690.
[38] S. Saloustros, L. Pelà, M. Cervera, P. Roca, Finite element modelling of internal and multiple localized cracks, Comput. Mech. 59 (2017) 299–316.
[39] S. Saloustros, L. Pelà, M. Cervera, A crack-tracking technique for localized cohesive–frictional damage, Eng. Fract. Mech. 150 (2015) 96–114.
[40] S. Saloustros, M. Cervera, L. Pelà, Tracking multi-directional intersecting cracks in numerical modelling of masonry shear walls under cyclic loading, Meccanica 53 (2018) 1757–1776.
[41] A. Rezaie, M. Godio, K. Beyer, Experimental investigation of strength, stiffness and drift capacity of rubble stone masonry walls, Constr. Build. Mater. 251 (2020) 118972, http://dx.doi.org/10.1016/j.conbuildmat.2020.118972, URL: http://www.sciencedirect.com/science/article/pii/S0950061820309776.
[42] A. Rezaie, R. Achanta, M. Godio, K. Beyer, Comparison of crack segmentation using digital image correlation measurements and deep learning, Constr. Build. Mater. 261 (2020) 120474, http://dx.doi.org/10.1016/j.conbuildmat.2020.120474, URL: http://www.sciencedirect.com/science/article/pii/S095006182032479X.

[43] A. Anthoine, G. Magonette, G. Magenes, Shear–compression testing and analysis of brick masonry walls, in: Proceedings of the 10th European Conference on Earthquake Engineering, vol. 3, 1995, pp. 1657–1662.

[44] A.H. Salmanpour, N. Mojsilović, J. Schwartz, Displacement capacity of contemporary unreinforced masonry walls: An experimental study, Eng. Struct. 89 (2015) 1–16.

[45] F. Vanin, D. Zaganelli, A. Penna, K. Beyer, Estimates for the stiffness, strength and drift capacity of stone masonry walls based on 123 quasi-static cyclic tests reported in the literature, Bull. Earthq. Eng. 15 (2017) 5435–5479, http://dx.doi.org/10.1007/s10518-017-0188-5.

[46] Correlated Solutions, VIC-3D Software Manual, 2018, http://dx.doi.org/10.32720/idics/gpg.ed1.

[47] Y.-J. Cha, W. Choi, O. Büyüköztürk, Deep learning-based crack damage detection using convolutional neural networks, Comput.-Aided Civ. Infrastruct. Eng. 32 (2017) 361–378.

[48] Q. Zou, Z. Zhang, Q. Li, X. Qi, Q. Wang, S. Wang, S. Member, DeepCrack : Learning hierarchical convolutional features for crack detection, IEEE Trans. Image Process. 28 (2019) 1498–1512, http://dx.doi.org/10.1109/TIP.2018.2878966.

[49] D. Dais, İhsan Engin Bal, E. Smyrou, V. Sarhosis, Automatic crack classification and segmentation on masonry surfaces using convolutional neural networks and transfer learning, Autom. Constr. 125 (2021) 103606, http://dx.doi.org/10.1016/j.autcon.2021.103606, URL: https://www.sciencedirect.com/science/article/pii/S0926580521000571.

[50] Z. Liu, Y. Cao, Y. Wang, W. Wang, Computer vision-based concrete crack detection using U-net fully convolutional networks, Autom. Constr. 104 (2019) 129–139, http://dx.doi.org/10.1016/j.autcon.2019.04.005, URL: http://www.sciencedirect.com/science/article/pii/S0926580519301244.

[51] A. Mosinska, P. Marquez-Neila, M. Koziński, P. Fua, Beyond the pixel-wise loss for topology-aware delineation, in: Proceedings of the IEEE Conference on Computer Vision and Pattern Recognition, 2018, pp. 3136–3145, URL: http://openaccess.thecvf.com/content_cvpr_2018/html/Mosinska_Beyond_the_Pixel-Wise_CVPR_2018_paper.html.

[52] K. Chaiyasarn, W. Khan, L. Ali, M. Sharma, D. Brackenbury, M. Dejong, Crack detection in masonry structures using convolutional neural networks and support vector machines, in: J. Teizer (Ed.), Proceedings of the 35th International Symposium on Automation and Robotics in Construction, ISARC, International Association for Automation and Robotics in Construction (IAARC), Taipei, Taiwan, 2018, pp. 118–125, http://dx.doi.org/10.22260/ISARC2018/0016.

[53] O. Ronneberger, P. Fischer, T. Brox, U-net: Convolutional networks for biomedical image segmentation, in: International Conference on Medical Image Computing and Computer-Assisted Intervention, Springer, 2015, pp. 234–241.

[54] K. Simonyan, A. Zisserman, Very deep convolutional networks for large-scale image recognition, in: International Conference on Learning Representations, 2015, URL: https://arxiv.org/abs/1409.1556.

[55] O. Russakovsky, J. Deng, H. Su, J. Krause, S. Satheesh, S. Ma, Z. Huang, A. Karpathy, A. Khosla, M. Bernstein, A.C. Berg, L. Fei-Fei, Imagenet large scale visual recognition challenge, Int. J. Comput. Vis. 115 (2015) 211–252, http://dx.doi.org/10.1007/s11263-015-0816-y.

[56] S. Van der Walt, J.L. Schönberger, J. Nunez-Iglesias, F. Boulogne, J.D. Warner, N. Yager, E. Gouillart, T. Yu, Scikit-image: Image processing in Python, PeerJ 2 (2014) e453.

[57] L.P. Coelho, Mahotas: Open source software for scriptable computer vision, 2012, arXiv preprint arXiv:1211.4907.

[58] R.M. Haralick, S.R. Sternberg, X. Zhuang, Image analysis using mathematical morphology, IEEE Trans. Pattern Anal. Mach. Intell. PAMI-9 (1987) 532–550, http://dx.doi.org/10.1109/TPAMI.1987.4767941.

[59] N. Gehri, J. Mata-Falcón, W. Kaufmann, Automated crack detection and measurement based on digital image correlation, Constr. Build. Mater. 256 (2020) 119383, http://dx.doi.org/10.1016/j.conbuildmat.2020.119383, URL: http://www.sciencedirect.com/science/article/pii/S095006182031388X.

[60] M.A. Sutton, J.J. Orteu, H. Schreier, Image Correlation for Shape, Motion and Deformation Measurements: Basic Concepts, Theory and Applications, Springer Science & Business Media, 2009.

[61] B.V. Wilding, K.M. Dolatshahi, K. Beyer, Influence of load history on the force-displacement response of in-plane loaded unreinforced masonry walls, Eng. Struct. 152 (2017) 671–682, http://dx.doi.org/10.1016/j.engstruct.2017.09.038.